Hindawi
Journal of Sensors
Volume 2020, Article ID 2530257, 6 pages
https://doi.org/10.1155/2020/2530257

Research Article

Interferometer-in-Spectrometer for High-Resolution Optical Coherence Tomography

Lishuang Liu,[1] **Jun Xie**,[2] **Linbo Liu**,[2,3] **and Si Chen**[2]

[1]*School of Instrumentation Science & Optoelectronics Engineering, Beijing Information Science & Technology University, Beijing 100192, China*
[2]*School of Electrical & Electronic Engineering, Nanyang Technological University, Singapore, Singapore 639798*
[3]*School of Chemical & Biological Engineering, Nanyang Technological University, Singapore, Singapore 639798*

Correspondence should be addressed to Si Chen; chen1069@e.ntu.edu.sg

Received 4 June 2019; Revised 21 November 2019; Accepted 17 December 2019; Published 4 January 2020

Academic Editor: Qiang Wu

Ultrahigh-resolution optical coherence tomography provides an axial resolution of 1-2 μm for resolving cellular structures of biological tissues critical for the diagnosis of diseases. However, it requires a relatively large spectral bandwidth which is not supported by the key components of the imaging system. We propose a novel spectral-domain OCT design, termed interferometer-in-spectrometer, which is able to compensate the bandwidth limitations of the grating and the line scan sensor by spectral shaping without compromising the signal intensity and adding the system cost. The advantage of axial resolution and ranging depth over the standard design is experimentally validated using the standard testing method and fresh swine cornea ex vivo. Moreover, opportunities that opened up by this new scheme for improving the performances of spectral-domain OCT are also discussed.

1. Introduction

Optical coherence tomography (OCT) is a noninvasive cross-sectional optical imaging tool, which has been established as a routine diagnostic tool in ophthalmology [1–3], and a new clinical research tool in intravascular imaging [4–6], endoscopic imaging of gastrointestinal tracts [7–9], and respiratory tracts [10, 11]. One of the key advantages of OCT over the existing noninvasive imaging tools, such as magnetic resonance imaging, computed tomography, and ultrasound, is the ability to provide microscopic spatial resolutions that are comparable to histology [5, 9, 12]. In OCT, the axial resolution and the transverse resolution are normally decoupled: the transverse resolution is determined by the effective numerical aperture of the sample arm focusing optics; the axial resolution is related with the center wavelength and power spectral density profile of the detected interference signal since the axial point-spread function is the Fourier transform of the power spectrum of the detected interference signal. Assuming a Gaussian power spectral density profile, the full-width at the half-maximum (FWHM) axial resolution can be calculated as $\delta = 0.44\lambda_c^2/\Delta\lambda$, where λ_c is the center wavelength and $\Delta\lambda$ is the FWHM spectral bandwidth [13]. In the time-domain OCT, maintaining a high spectral bandwidth of the detected signal is relatively straightforward since the detectors are photodiodes. In this case, typically, the spectral response of available photodiodes is broad enough to support ultrahigh-resolution OCT, and there is no aberration issues and other band-limiting components [12]. However, it is challenging to maintain a highly detected spectral bandwidth in the Fourier domain OCT, which has replaced its predecessor due to the three orders of magnitude higher sensitivity or speed advantage.

There are two types of Fourier domain OCT: swept-source OCT and spectral-domain OCT (SD-OCT). The former is becoming more and more popular owning to its superior instantaneous spectral line width and line rate over the latter. However, it is very difficult, if possible, to achieve an ultrahigh axial resolution (1-2 μm) using a swept source, because of the limitation of the gain medium in the spectral

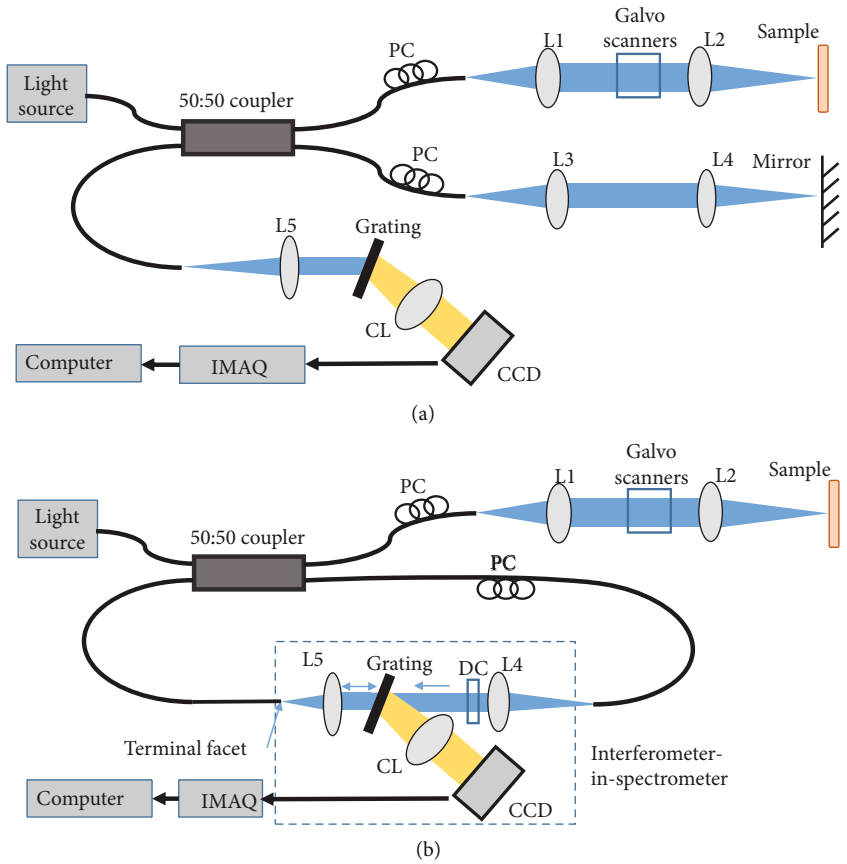

Figure 1: Schematics of ultrahigh-resolution OCT. (a) Standard scheme; (b) IIS scheme. PC: polarization controller; CL: camera lens; CCD: charge coupled device (line scan camera); DC: dispersion compensator; IMAQ: image acquisition module.

bandwidth (up to 140 nm) [14]. As a result, SD-OCT is the only form to realize ultrahigh or cellular resolution imaging [5, 15–17]. Although broadband light sources are available, the fiber coupler and spectrometer are the most significant bandwidth-limiting devices in SD-OCT, which may compromise the axial resolution or the ranging depth. Specifically, currently available fused fiber couplers, gratings, and line scan cameras are limited in the spectral bandwidth [18] which suffer from trade-offs between the detected spectral bandwidth and the spectrometer efficiency. For example, the Si-based camera has a poor response above ~900 nm and InGaAs-based camera is particularly suboptimal in the spectral region under 950 nm. As a result, in order to maintain a detected spectral bandwidth high enough to support an ultrahigh axial resolution (1-2 μm), the detection sensitivity has to be sacrificed which is not viable for clinical applications.

A straightforward solution is to use a spectral shaping measure to compensate for the bandwidth limitation. Apparently, it is not reasonable to shape the detected light from the sample since the scattered power budget is extremely tight. Shaping the input light is not desired since it is not power economical. The only light that can be sacrificed is that in the reference beam simply because in a typical OCT, the majority of light allocated to the reference arm is wasted (Figure 1(a)). Therefore, one can insert a spectral shaper in the reference arm to improve the axial resolution without compromising the detection sensitivity. However, a more cost-effective solution is to use the grating in the spectrometer as the spectral shaper. In this study, we have developed a novel SD-OCT which integrated the interferometer into the spectrometer, termed interferometer-in-spectrometer (IIS) scheme. IIS scheme uses the grating in the spectrometer as the spectral shaper and the terminal facet of the core of the spectrometer input fiber as the interferometer, so that the reference spectrum can be shaped to compensate the limited spectral bandwidth of the sample light through interference. IIS scheme provides a platform that can support other optical manipulations for improving performance of SD-OCT.

2. Materials and Methods

We used a previously reported ultrahigh-resolution OCT system as the benchmark [19]. Shown in Figure 1(a), a broadband light source (Superlum Broadlighters T-850-HP, Ireland) with a center wavelength of 850 nm and a FWHM bandwidth of 165 nm was used. The source output was split by a broadband 50 : 50 fiber coupler (TW850R5A2, Thorlabs Inc., USA) to the sample arm and the reference arm. The sample arm consisted of a collimation lens L1 (LA4647-B, Thorlabs Inc., USA), a galvo scanner (GVSM002/M, Thorlabs Inc., USA), and an objective lens L2 (AC127-030-B, Thorlabs Inc., USA). The reference arm was equipped with

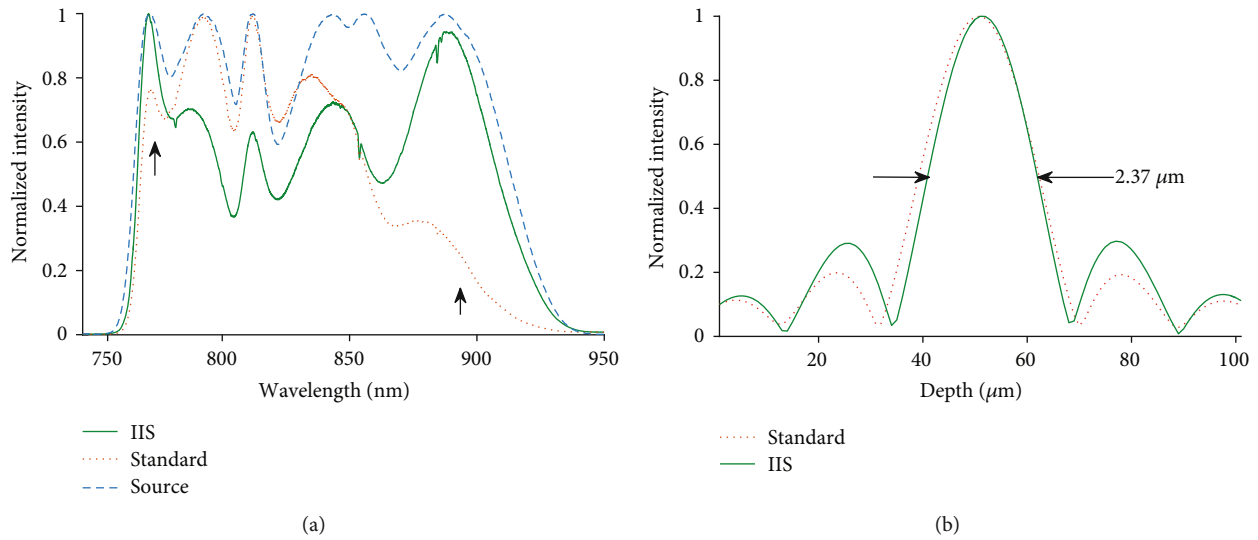

Figure 2: Detected spectra and axial point-spread functions. (a) The detected spectra from the standard scheme (red dotted curve) and the IIS scheme (green solid curve). The blue dashed curve represents the source spectrum. The arrows indicate the locations of the spectrum that were affected by both the camera response and the grating transmission efficiency. (b) The measured axial point-spread functions of the standard scheme (red dotted curve) and the IIS scheme (green solid curve). The depth scales are in air.

the same refractive optics as the sample arm. The spectrometer was composed of a collimation lens L5 (AC127-030-B, Thorlabs Inc., USA), a grating (1200 l/mm, Wasatch Photonics Inc., USA), a camera lens (Nikon AF Nikkor 85 mm f/1.8D), and a line scan camera (CCD, E2V, EV71YEM4CL2014-BA9) with a pixel size of 14 μm × 28 μm (width × height) and a pixel number of 2048.

In the IIS scheme, the reference light was collimated by L4 before being fed to the spectrometer through the zero-order diffraction channel of the grating (Figure 1(b)). Since L4 and L5 were identical, the focal spots of the reference beam and the back-reflected or back-scattered sample beam overlapped perfectly at the terminal facet of the core of the spectrometer input fiber, so that the interferometer was integrated in the spectrometer. The fiber terminal is flat-polished so that the reference light reflected by the fiber terminal facet and the sample light transmitted through the fiber terminal facet propagated along the same direction. The interference light was collimated by L5 and directed to the line scan camera through the grating and the camera lens. The optical power from the reference fiber was measured to be 8 mW, which was attenuated to ~400 μW by the grating and further to ~16 μW by the fiber terminal facet reflection. A reference power of ~16 μW is more than enough to support a line scan rate of up to 50 kHz. In our experimental setup, both schemes shared the same sample arm and the spectrometer so that the measured results can be directly compared without any bias.

3. Results and Discussion

The spectrum of the light source was in an approximately top-hat shape with uniform power density of all the peaks (Figure 2(a), blue dashed curve). However, due to the bandwidth limitations of the system components, in the standard scheme, the detected spectrum has deteriorated (Figure 2(a), red dotted curve) with 40% smaller bandwidth and blue-shifted center wavelength. Consequently, the axial resolution was measured to be 2.55 μm in air (Figure 2(b), red dotted curve). In the IIS scheme, the reference light passed through the zero-order channel of the grating. The detected reference spectrum (Figure 2(a), green solid curve) had a spectral shape of a notch filter, indicating that there is much higher transmission efficiency in the short and long ends of the spectrum than in the center. Since the interference signal intensity is the product of the power spectral density of the two arms, the interference spectral bandwidth was restored. The axial resolution obtained by IIS scheme was measured to be 2.37 μm in air (Figure 2(b), green solid curve), which is ~10% higher than the standard scheme.

We investigated the spectral modulation effects of the system components either through the data provided by the manufacturer or using a spectral analyzer (AQ6370C, YOKOGAWA). Firstly, we measured the spectra at the fiber tip of the reference arm in the standard (Figure 1(a)) and the IIS scheme (Figure 1(b)), and the data is shown as the red dashed curve and the blue solid curve in Figure 3(a), respectively. In the single-pass spectrum (IIS scheme), the short and long wavelength portions suffer more coupling loss than the central portion, due to the bandpass filter behavior of the port-to-port coupling ratio (black dash-botted curve), so that the overall bandwidth is reduced. In the double-pass spectrum (the standard scheme), the long wavelength portion suffers the same coupling loss as the center part, which is apparently due to the fact that the double-pass coupling ratio is uniform from across the single-mode operation region (green dotted curve). However, the short wavelength portion suffers much more loss than the single-pass case due to the doubled multimode loss. In summary, the spectral modulation of the fused fiber coupler contributed partly to the bandwidth limitation of the high-resolution OCT systems.

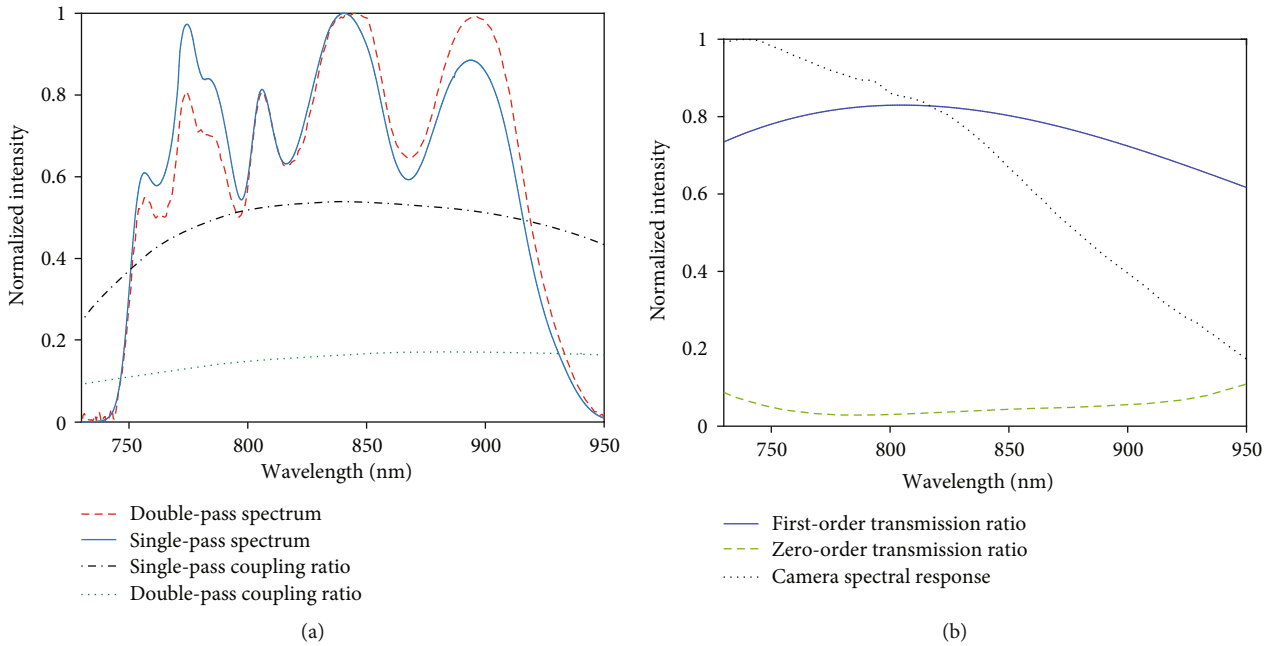

Figure 3: Spectral modulation effects of the system components. (a) Spectral coupling ratios and reference light spectra with and without back-coupling through the fused fiber coupler. (b) Spectral response of the camera and transmission efficiencies of the grating.

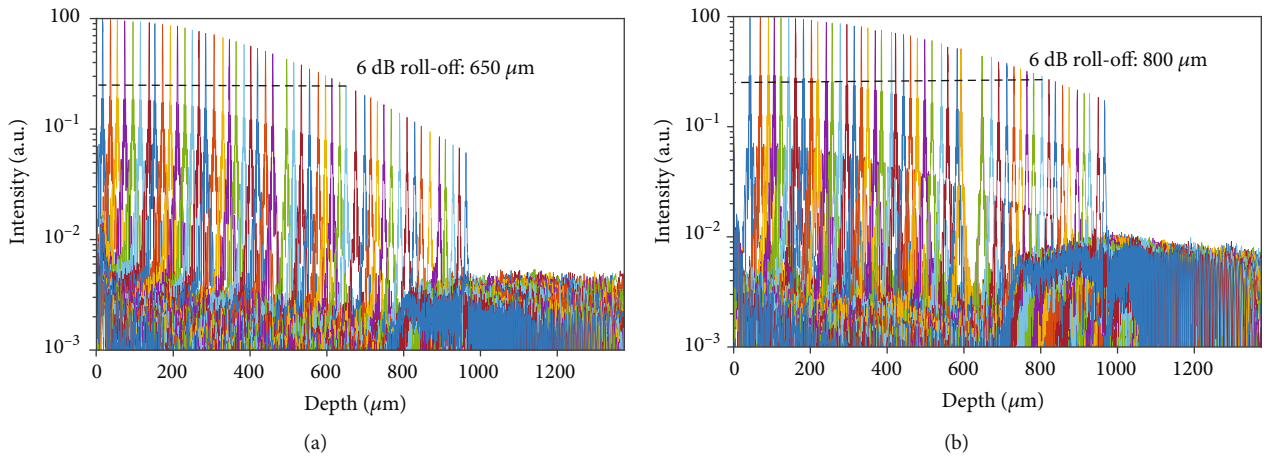

Figure 4: Axial point-spread functions over depth detected by changing the optical path length difference between the sample and the reference arms. (a) Axial point-spread functions of the standard scheme showing a 6 dB intensity roll-off range of 650 μm in the tissue (refractive index = 1.38). (b) Axial point-spread functions of the IIS scheme showing a 6 dB intensity roll-off range of 800 μm in the tissue (refractive index = 1.38).

More importantly, the spectral response of the camera (Figure 3(b), black dotted curve) decreased approximately linearly from the short wavelength (~750 nm) to the long wavelength (~950 nm) by ~75%. To make things worse, the first order diffraction efficiency of the grating is essentially a spectral bandpass curve (blue solid curve). All these bandpass effects mentioned above can be compensated by passing the reference light through the zero-order channel of the grating, which has a spectral notch filter effect (green dashed curve).

Note that because the blue shift of the center wavelength, in the standard scheme, the axial resolution did not drop as much as the detected spectral bandwidth. However, the price to pay is the shorter ranging depth due to the large attenuation in the long wavelength region (Figure 2(a)). The measured 6 dB intensity roll-off was at 800 μm in the tissue (refractive index = 1.38) for the standard scheme, which was 150 μm longer than that in the standard scheme (Figure 4).

In order to demonstrate the imaging capability of IIS scheme, we acquired images of swine cornea using both the standard and the IIS scheme *ex vivo*. The swine eyes were harvested freshly from a local slaughterhouse and were maintained in neutral-buffered phosphate-buffered saline during the transportation. The imaging experiments were conducted after 3-4 hours postmortem. We used an A line rate of 20 k Hz and a frame rate of 20 Hz. The transverse scanning range was 2.616 mm. In the image acquired using the

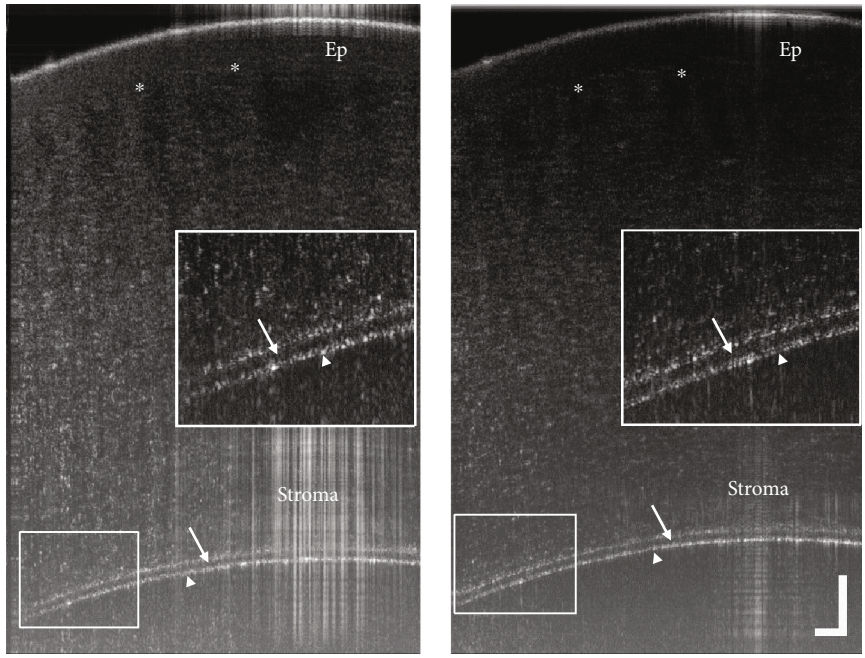

(a) (b)

Figure 5: Cross-sectional images of the swine cornea *ex vivo*. (a) A representative image acquired by the standard scheme where the endothelium layer (arrowheads) was not clearly resolved. (b) The corresponding image acquired by the IIS scheme where the endothelium layer was clearly resolved by two interfaces (arrowheads). Ep: corneal epithelium; asterisks: interface between the corneal epithelium and the stroma; arrows: Descemet's membrane. Insets: 2× magnified view of the region in the box. Scale bars: 100 μm in the tissue (refractive index = 1.38).

standard scheme (Figure 5(a)), some corneal layers can be identified, including the epithelium (Ep), stroma, and the Descemet's membrane (arrows). However, the corneal endothelium cannot be clearly resolved (arrowheads). In the image acquired using the IIS scheme (Figure 5(b)), this thin single layer of squamous cells can be clearly identified by two interfaces (arrowheads in inset): the anterior interface between the Descemet's membrane (arrows) and the endothelium and the posterior interface between the endothelium and the aqueous humor in the anterior chamber. These results demonstrated that the axial resolution restored by IIS scheme improved the capability of the ultrahigh-resolution OCT.

IIS scheme is a novel platform of spectral-domain OCT that can potentially accommodate more reference beam manipulation techniques, in addition to spectral shaping. Multielement camera lenses may be well corrected for optical aberrations in the spectrometer, but multiple surface reflections cause the problem of low light throughput, especially for the very low-intensity optical signals back-scattered from the sample. In addition, the high-profile multielement lenses and antireflection coatings are also very expensive. One can insert low-cost aberration correction optics in the reference path of the IIS to compensate the aberrations of the camera lens, without introducing additional loss to the sample signal. In most of OCT systems, signal mode fibers are used so that the spot size at the line scan camera is proportional to the wavelength, leading to suboptimal roll-off performance at the long wavelengths in a linear-k spectrometer [20]. To mitigate this issue, one can use an endlessly signal mode photonics crystal fiber [21] in the reference arm to achieve a uniform spot size at the line scan camera over the entire spectral range. Although there will be coupling loss between the signal mode fiber and the endlessly signal mode photonics crystal fiber due to numerical aperture mismatch, only the reference beam will be affected which can be tolerated within the optical power budget. However, there are some drawbacks of the IIS scheme. Firstly, it involves fiber pinhole coupling optics for the reference beam to overlap with the sample beam at the core of the spectrometer fiber terminal facet. This additional free space optics adds complexity and alignment difficulty with regard to the standard spectrometer. Secondly, it is difficult to tailor the spectral shape in this study which unavoidably is associated with the side lobe problem.

4. Conclusions

In conclusion, we report a novel spectral-domain OCT design: interferometer-in-spectrometer scheme, which makes it possible to manipulate the reference beam for improved performances without compromising the signal intensity or significantly increasing the system cost. Our spectral shaping experiments validated the advantages of the new scheme and improving axial resolution and ranging depth. Further studies are needed to full explore the possibilities opened up by this new scheme, such as aberration correction and improving the spot size of the spectrometer optics.

Data Availability

The data used to support the findings of this study are available from the corresponding author upon request.

Conflicts of Interest

The authors declare that there is no conflict of interest regarding the publication of this paper.

Acknowledgments

This research is supported by Beijing Natural Science Foundation (7172035).

References

[1] W. Drexler, U. Morgner, R. K. Ghanta, F. X. Kartner, J. S. Schuman, and J. G. Fujimoto, "Ultrahigh-resolution ophthalmic optical coherence tomography," *Nature Medicine*, vol. 7, no. 4, pp. 502–507, 2001.

[2] J. G. Fujimoto, "Optical coherence tomography for ultrahigh resolution in vivo imaging," *Nature Biotechnology*, vol. 21, no. 11, pp. 1361–1367, 2003.

[3] J. G. Fujimoto, M. E. Brezinski, G. J. Tearney et al., "Optical biopsy and imaging using optical coherence tomography," *Nature Medicine*, vol. 1, no. 9, pp. 970–972, 1995.

[4] H. Yoo, J. W. Kim, M. Shishkov et al., "Intra-arterial catheter for simultaneous microstructural and molecular imaging in vivo," *Nature Medicine*, vol. 17, no. 12, pp. 1680–1684, 2011.

[5] L. Liu, J. A. Gardecki, S. K. Nadkarni et al., "Imaging the subcellular structure of human coronary atherosclerosis using micro-optical coherence tomography," *Nature Medicine*, vol. 17, no. 8, pp. 1010–1014, 2011.

[6] C. P. Fleming, J. Eckert, E. F. Halpern, J. A. Gardecki, and G. J. Tearney, "Depth resolved detection of lipid using spectroscopic optical coherence tomography," *Biomedical Optics Express*, vol. 4, no. 8, pp. 1269–1284, 2013.

[7] M. J. Suter, M. J. Gora, G. Y. Lauwers et al., "Esophageal-guided biopsy with volumetric laser endomicroscopy and laser cautery marking: a pilot clinical study," *Gastrointestinal Endoscopy*, vol. 79, no. 6, pp. 886–896, 2014.

[8] J. M. Poneros, S. Brand, B. E. Bouma, G. J. Tearney, C. C. Compton, and N. S. Nishioka, "Diagnosis of specialized intestinal metaplasia by optical coherence tomography," *Gastroenterology*, vol. 120, no. 1, pp. 7–12, 2001.

[9] S. Chen, X. Ge, X. Liu et al., "Understanding optical reflectance contrast for real-time characterization of epithelial precursor lesions," *Bioengineering & Translational Medicine*, vol. 4, no. 3, article e10137, 2019.

[10] L. Liu, K. K. Chu, G. H. Houser et al., "Method for quantitative study of airway functional microanatomy using micro-optical coherence tomography," *PLoS One*, vol. 8, no. 1, article e54473, 2013.

[11] K. K. Chu, C. Unglert, T. N. Ford et al., "In vivo imaging of airway cilia and mucus clearance with micro-optical coherence tomography," *Biomedical optics express*, vol. 7, no. 7, pp. 2494–2505, 2016.

[12] S. A. Boppart, B. E. Bouma, C. Pitris, J. F. Southern, M. E. Brezinski, and J. G. Fujimoto, "In vivo cellular optical coherence tomography imaging," *Nature Medicine*, vol. 4, no. 7, pp. 861–865, 1998.

[13] J. M. Schmitt, "Optical coherence tomography (OCT): a review," *IEEE Journal of Selected Topics in Quantum Electronics*, vol. 5, no. 4, pp. 1205–1215, 1999.

[14] J. P. Kolb, T. Pfeiffer, M. Eibl, H. Hakert, and R. Huber, "High-resolution retinal swept source optical coherence tomography with an ultra-wideband Fourier-domain mode-locked laser at MHz A-scan rates," *Biomedical Optics Express*, vol. 9, no. 1, pp. 120–130, 2018.

[15] S. Chen, X. Liu, N. Wang et al., "Visualizing Micro-anatomical Structures of the Posterior Cornea with Micro- optical Coherence Tomography," *Scientific reports*, vol. 7, no. 1, article 10752, 2017.

[16] X. Liu, S. Chen, D. Cui, X. Yu, and L. Liu, "Spectral estimation optical coherence tomography for axial super-resolution," *Optics express*, vol. 23, no. 20, pp. 26521–26532, 2015.

[17] X. Yao, Y. Gan, C. C. Marboe, and C. P. Hendon, "Myocardial imaging using ultrahigh-resolution spectral domain optical coherence tomography," *Journal of Biomedical Optics*, vol. 21, no. 6, article 61006, p. 061006, 2016.

[18] D. Cui, X. Liu, J. Zhang et al., "Dual spectrometer system with spectral compounding for 1-μm optical coherence tomography *in vivo*," *Optics Letters*, vol. 39, no. 23, pp. 6727–6730, 2014.

[19] X. Yu, Q. Xiong, Y. Luo et al., "Contrast enhanced subsurface fingerprint detection using high-speed optical coherence tomography," *IEEE Photonics Technology Letters*, vol. 29, no. 1, pp. 70–73, 2017.

[20] G. Lan and G. Li, "Design of a *k*-space spectrometer for ultra-broad waveband spectral domain optical coherence tomography," *Scientific Reports*, vol. 7, no. 1, article 42353, 2017.

[21] T. A. Birks, J. C. Knight, and P. S. J. Russell, "Endlessly single-mode photonic crystal fiber," *Optics Letters*, vol. 22, no. 13, pp. 961–963, 1997.